JCTC Journal of Chemical Theory and Computation

pubs.acs.org/JCTC Article

Electronic Dynamics through Conical Intersections via Quasiclassical Mapping Hamiltonian Methods

Yudan Liu, Xing Gao, Yifan Lai, Ellen Mulvihill, and Eitan Geva*

Cite This: https://dx.doi.org/10.1021/acs.jctc.0c00177 Read Online

ACCESS | Metrics & More | Article Recommendations

ABSTRACT: In this work, we investigate the ability of different quasiclassical mapping Hamiltonian methods to simulate the dynamics of electronic transitions through conical intersections. The analysis is carried out within the framework of the linear vibronic coupling (LVC) model. The methods compared are the Ehrenfest method, the symmetrical quasiclassical method, and several variations of the linearized semiclassical (LSC) method, including ones that are based on the recently introduced modified representation of the identity operator. The accuracy of the various methods is tested by comparing their predictions to quantum-mechanically exact results obtained via the multiconfiguration time-dependent Hartree (MCTDH) method. The LVC model is found to be a nontrivial benchmark model that can differentiate between different approximate methods based on their accuracy better than previously used benchmark models. In the three systems studied, two of the LSC methods are found to provide the most accurate description of electronic transitions through conical intersections.

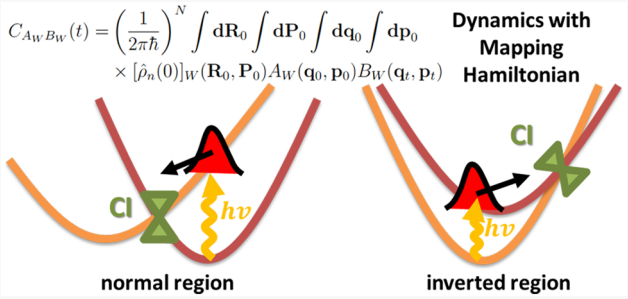

1. INTRODUCTION

Conical intersections (CIs) are believed to play a central role in many photochemical processes.[1−12] Being able to calculate the rates of electronic transitions through CIs in a reliable and feasible manner is therefore key for understanding such processes and developing rational design principles toward controlling them. An exact fully quantum-mechanical simulation of the dynamics of electronic transitions through CIs is limited to relatively low-dimensional molecular systems or simple model Hamiltonians.[13−16] Thus, developing approximate methods for simulating the dynamics of electronic transitions through CIs in complex molecular systems is highly desirable.

A wide variety of approximate methods that can be used for simulating nonadiabatic dynamics in systems with CIs have been proposed, including the Ehrenfest (mean-field) method,[17] surface hopping methods,[18−29] the mixed quantum-classical Liouville (MQCL) method,[30−37] and mapping Hamiltonian (MH) approaches.[13,37−55] These approximate methods reduce the computational cost by describing the dynamics of the nuclear degrees of freedom (DOF), and sometimes also of the electronic DOF, in terms of classical-like trajectories.

Approximate methods based on combining the MH approach with quasiclassical (QC) approximations have recently emerged as a promising approach toward modeling nonadiabatic dynamics in complex molecular systems.[49,56] Several variations of those QC/MH methods have been found to be accurate for a variety of benchmark models, including the spin-boson model, a Frenkel biexciton model, Tully models, and a model for the Fenna−Matthews−Olson (FMO) light-harvesting complex.[49] Importantly, none of those models include CIs. Our goal in this work is to extend the range of applications of QC/MH methods to systems with CIs. We do so in the context of the linear vibronic coupling (LVC) model Hamiltonian.[3,57] The choice of the LVC model Hamiltonian as a benchmark for testing the ability of QC/MH methods to describe the dynamics of electronic transitions through CIs is motivated by the fact that it has been reported to provide a rather accurate description of CI photophysics in many polyatomic molecules and by the ability to calculate quantum-mechanically exact electronic transition rates for it. The analysis was performed on LVC Hamiltonians parametrized for three polyatomic systems: fulvene, the 2,6-bis(methylene) adamantyl (BMA) radical cation, and the 2-methylene-6-isopropylidene adamantyl (MIA) radical cation. The choice of these systems was motivated by the availability of ab initio parameter sets and the fact that these systems were used in the past as benchmarks for equilibrium Fermi's golden rule (EQ-FGR), nonequilibrium Fermi's golden rule (NE-

Received: February 20, 2020
Published: May 18, 2020

FGR) and linearized semiclassical (LSC) approximations with EQ-FGR and NE-FGR.[5,58] It should also be noted that these systems represent the inverted region (fulvene), normal region (BMA), and the vicinity of the transition point between those two regions (MIA).

The rest of the article is organized as follows. The LVC model and choice of initial state are described in section 2. The various QC/MH methods tested and compared are outlined in section 3. The results obtained by applying those QC/MH methods to the aforementioned molecular systems described by the LVC Hamiltonian are reported in section 4. Discussion of the results is given in section 5. Concluding remarks are given in section 6.

2. THE LINEAR VIBRONIC COUPLING (LVC) MODEL AND CHOICE OF INITIAL STATE

The LVC model Hamiltonian is given by[3,57]

$$\hat{H} = \hat{H}_1|1\rangle\langle 1| + \hat{H}_2|2\rangle\langle 2| + V_{12}(\hat{\mathbf{R}})|1\rangle\langle 2| + V_{21}(\hat{\mathbf{R}})|2\rangle\langle 1| \tag{1}$$

where

$$\hat{H}_j = \frac{\hat{\mathbf{P}}^2}{2} + V_{jj}(\hat{\mathbf{R}}),$$
$$V_{jj}(\hat{\mathbf{R}}) = \Delta_j + \sum_{i=1}^{N_n} \frac{1}{2}\omega_i^2 \hat{R}_i^2 + d_i^{(j)}\hat{R}_i,$$
$$V_{12}(\hat{\mathbf{R}}) = V_{21}(\hat{\mathbf{R}}) = \sum_{i=1}^{N_n} c_i \hat{R}_i. \tag{2}$$

$\hat{H}_j$ represents the nuclear Hamiltonian when the system is in the electronic state $|j\rangle$ (j = 1, 2), $V_{12}(\hat{\mathbf{R}}) = V_{21}(\hat{\mathbf{R}})$ are the coupling terms between the two electronic states, and N_n is the number of nuclear DOF. Boldfaced variables, for example, $\mathbf{A}$, indicate vector quantities, and a hat over a variable, for example, $\hat{B}$, indicates an operator quantity.

Within the LVC Hamiltonian, eq 1, the nuclear DOF are given in terms of their mass-weighted coordinates, $\hat{\mathbf{R}} = (\hat{R}_1, ..., \hat{R}_{N_n})$, and momenta, $\hat{\mathbf{P}} = (\hat{P}_1, ..., \hat{P}_{N_n})$. Importantly, the diabatic potential energy surfaces (PESs), $V_{jj}(\hat{\mathbf{R}})$, are assumed to be harmonic and identical, except for a shift in equilibrium energy and geometry. The electronic coupling terms, $V_{12}(\hat{\mathbf{R}}) = V_{21}(\hat{\mathbf{R}})$, are assumed to be linear in the nuclear coordinates. The fact that the electronic coupling terms are explicitly $\hat{\mathbf{R}}$-dependent (i.e., in the non-Condon regime) is what makes it possible for the LVC Hamiltonian to account for CIs.

We also note for future reference that the reaction free energy and reorganization energy for the LVC model are given by

$$\Delta E = \Delta_1 - \Delta_2 - \sum_{i=1}^{N_n} \frac{(d_i^{(1)})^2 - (d_i^{(2)})^2}{2\omega_i^2},$$
$$E_r = \sum_{i=1}^{N_n} \frac{(d_i^{(1)} - d_i^{(2)})^2}{2\omega_i^2} \tag{3}$$

$E_r > |\Delta E|$ and $E_r < |\Delta E|$ correspond to the Marcus normal and inverted regions, respectively.

In what follows, we assume that the initial state of the overall system is given by

$$\hat{\rho}(0) = \hat{\rho}_n(0) \otimes \hat{\sigma}(0) \tag{4}$$

where $\hat{\rho}_n(0)$ and $\hat{\sigma}(0)$ are the reduced density operators that describe the initial states of the nuclear DOF and electronic DOF, respectively. The initial electronic state, $\hat{\sigma}(0)$, is assumed to be given by $|1\rangle\langle 1|$ or $|2\rangle\langle 2|$. The initial nuclear state, $\hat{\rho}_n(0)$, is assumed to be given by $\hat{\rho}_n(0) = e^{-\beta\hat{H}_2}/\mathrm{Tr}\{e^{-\beta\hat{H}_2}\}$ if $\hat{\sigma}(0) = |1\rangle\langle 1|$ or $\hat{\rho}_n(0) = e^{-\beta\hat{H}_1}/\mathrm{Tr}\{e^{-\beta\hat{H}_1}\}$ if $\hat{\sigma}(0) = |2\rangle\langle 2|$. Here, $\beta = 1/(k_B T)$ where T is the absolute temperature and k_B is the Boltzmann constant. It should be noted that this choice corresponds to a *nonequilibrium* initial state since the nuclear DOF are in equilibrium with respect to one electronic state while the electronic DOF are described by the other state.

The electronic density operator at a later time t is given by

$$\hat{\sigma}(t) = \sigma_{11}(t)|1\rangle\langle 1| + \sigma_{22}(t)|2\rangle\langle 2| + \sigma_{12}(t)|1\rangle\langle 2| + \sigma_{21}(t)|2\rangle\langle 1| \tag{5}$$

where

$$\sigma_{jk}(t) = \mathrm{Tr}\{\hat{\rho}_n(0)|\alpha\rangle\langle\alpha| e^{i\hat{H}t/\hbar}|k\rangle\langle j| e^{-i\hat{H}t/\hbar}\} \tag{6}$$

Here, $\hat{\rho}_n(0)|\alpha\rangle\langle\alpha|$ is the aforementioned nonequilibrium initial state. $\sigma_{jj}(t)$ corresponds to the population of the jth electronic state and $\sigma_{jk}(t)$ (where $j \neq k$) corresponds to the electronic coherence between the jth and the kth electronic states. It should be noted that the coherence, $\sigma_{21}(t)$, is relatively small ($\sim 10^{-3}$) for the systems under consideration in this article. As a result, getting converged results for the coherence would have required a significantly larger number of trajectories, which we felt was not justified, given that population transfer dynamics is often the main quantity of interest for systems with CIs. In what follows, we will focus on the population dynamics, that is, on the dynamics of $\sigma_{11}(t)$ and $\sigma_{22}(t)$.

As outlined in refs 48 and 49, the electronic population operator can also be mapped as the sum of the identity operator, $\hat{1}$, and a trace zero term, giving the alternative form

$$|a\rangle\langle a| \rightarrow \frac{1}{N_e}(\hat{1} + \hat{Q}_a) \tag{7}$$

where

$$\hat{Q}_a = N_e \hat{M}_{aa} - \sum_{b=1}^{N_e} \hat{M}_{bb} \tag{8}$$

in which $\hat{M}_{aa} \equiv |a\rangle\langle a|$ and N_e is the number of electronic DOF. Plugging eq 7 into eq 6 leads to the following alternative expressions for the electronic density matrix elements:

$$\sigma_{\lambda\lambda}(t) = \frac{1}{N_e^2}[N_e + C_{\hat{1}\hat{Q}_\lambda}(t) + C_{\hat{Q}_\alpha\hat{Q}_\lambda}(t)]$$
$$\sigma_{\lambda\zeta}(t) = \frac{1}{N_e}[C_{\hat{1}\hat{M}_{\zeta\lambda}}(t) + C_{\hat{Q}_\alpha\hat{M}_{\zeta\lambda}}(t)] \tag{9}$$

Here $\hat{M}_{\zeta\lambda} \equiv |\zeta\rangle\langle\lambda|$. The indices λ and ζ will be used consistently throughout this paper to indicate indices that are different ($\lambda \neq \zeta$). This should be contrasted to all other indices, for example, j and k, which can be equal unless explicitly stated otherwise.

3. THE MAPPING HAMILTONIAN (MH) APPROACH AND QUASICLASSICAL (QC) APPROXIMATIONS

MH methods are based on casting the population and coherence operators, $\{|j\rangle\langle k|\}$, onto an isomorphic set of operators, $\{M_{jk}(\hat{\mathbf{q}}, \hat{\mathbf{p}})\}$:

https://dx.doi.org/10.1021/acs.jctc.0c00177
J. Chem. Theory Comput. XXXX, XXX, XXX−XXX

$$|j\rangle\langle k| \rightarrow M_{jk}(\hat{\mathbf{q}}, \hat{\mathbf{p}}) \tag{10}$$

with $\{M_{jk}(\hat{\mathbf{q}}, \hat{\mathbf{p}})\}$ satisfying the same commutation relations as $\{|j\rangle\langle k|\}$.[13,39,41,48−54,54,55,59−66] Here, $\{\hat{\mathbf{q}}, \hat{\mathbf{p}}\}$ are a set of auxiliary Cartesian coordinate and momentum operators.

In terms of the mapping operators, casting the electronic density matrix elements in eq 6 yields

$$\sigma_{jk}(t) \equiv C_{\hat{M}_{\alpha\alpha}\hat{M}_{kj}}(t) \tag{11}$$

and in eq 9 yields

$$\sigma_{\lambda\lambda}(t) = \frac{1}{N_e^2}[N_e + C_{\hat{1}\hat{Q}_\lambda}(t) + C_{\hat{Q}_\alpha\hat{Q}_\lambda}(t)]$$
$$\sigma_{\lambda\zeta}(t) = \frac{1}{N_e}[C_{\hat{1}\hat{M}_{\zeta\lambda}}(t) + C_{\hat{Q}_\alpha\hat{M}_{\zeta\lambda}}(t)] \tag{12}$$

Here $\hat{Q}_a = N_e\hat{M}_{aa} - \sum_{b=1}^{N_e}\hat{M}_{bb}$, and the correlation function

$$C_{\hat{A}\hat{B}}(t) = \mathrm{Tr}\{\hat{\rho}_n(0)A(\hat{\mathbf{q}}(0), \hat{\mathbf{p}})B(\hat{\mathbf{q}}(t), \hat{\mathbf{p}}(t))\} \tag{13}$$

3.1. QC/MH Methods Based on the Linearized Semiclassical (LSC) Approximation. Applying the LSC approximation[67] to a correlation function of the form given in eq 13 results in the following QC approximation for $C_{\hat{A}\hat{B}}(t)$:

$$C_{A_WB_W}(t) = \left(\frac{1}{2\pi\hbar}\right)^N \int d\mathbf{R}_0 \int d\mathbf{P}_0 \int d\mathbf{q}_0 \int d\mathbf{p}_0 \times [\hat{\rho}_n(0)]_W(\mathbf{R}_0, \mathbf{P}_0)A_W(\mathbf{q}_0, \mathbf{p}_0)B_W(\mathbf{q}_t, \mathbf{p}_t) \tag{14}$$

Here, $N = N_e + N_n$ is the total number of DOF of the overall system. $[\hat{\rho}_n(0)]_W(\mathbf{R},\mathbf{P})$ is the Wigner transform of the nuclear operator, $\hat{\rho}_n(0)$. $A_W(\mathbf{q}_0, \mathbf{p}_0)$ and $B_W(\mathbf{q}_t, \mathbf{p}_t)$ are the Wigner transforms of the electronic operators $\hat{A}$ and $\hat{B}$, respectively. The general form of the Wigner transforms of a nuclear operator $\hat{D}$ and an electronic operator $\hat{F}$ are given by

$$D_W(\mathbf{R}, \mathbf{P}) = \int d\mathbf{Z}\, e^{-i\mathbf{Z}\mathbf{P}/\hbar}\left\langle \mathbf{R} + \frac{\mathbf{Z}}{2}|D(\hat{\mathbf{R}}, \hat{\mathbf{P}})|\mathbf{R} - \frac{\mathbf{Z}}{2}\right\rangle$$
$$F_W(\mathbf{q}, \mathbf{p}) = \int d\mathbf{z}\, e^{-i\mathbf{z}\mathbf{p}/\hbar}\left\langle \mathbf{q} + \frac{\mathbf{z}}{2}|F(\hat{\mathbf{q}}, \hat{\mathbf{p}})|\mathbf{q} - \frac{\mathbf{z}}{2}\right\rangle \tag{15}$$

Applying the QC approximation to the correlation functions in eqs 11 and 12 leads to two alternative QC/MH approximations for the electronic density matrix elements, detailed in the following.

The actual choice of mapping variables is not unique and multiple choices of mapping variables have been proposed and employed.[54,55,64−66,68] In this work, we consider two such choices, which are based on the Stock−Thoss−Meyer−Miller mapping[13,38] (the reader is referred to refs 69 and 56 for a more detailed discussion of these two choices). The first choice, which we refer to as *mapping no. 1*, leads to the following QC mapping variables:

$$[\hat{M}_{\lambda\lambda}]_W^{(I)}(\mathbf{q}, \mathbf{p}) = \frac{1}{2\hbar}(q_\lambda^2 + p_\lambda^2 - \hbar)$$
$$[\hat{M}_{\lambda\zeta}]_W^{(I)}(\mathbf{q}, \mathbf{p}) = \frac{1}{2\hbar}(q_\lambda - ip_\lambda)(q_\zeta + ip_\zeta) \tag{16}$$

The second choice, which we refer to as *mapping no. 2*, leads to the following QC mapping variables:

$$[\hat{M}_{\lambda\lambda}]_W^{(II)}(\mathbf{q}, \mathbf{p}) = \phi(\mathbf{q}, \mathbf{p})\left(q_\lambda^2 + p_\lambda^2 - \frac{\hbar}{2}\right)$$
$$[\hat{M}_{\lambda\zeta}]_W^{(II)}(\mathbf{q}, \mathbf{p}) = \phi(\mathbf{q}, \mathbf{p})(q_\lambda - ip_\lambda)(q_\zeta + ip_\zeta) \tag{17}$$

where

$$\phi(\mathbf{q}, \mathbf{p}) = \frac{2^{N_e+1}}{\hbar}\exp\left[-\frac{1}{\hbar}\sum_{l=1}^{N_e}(q_l^2 + p_l^2)\right] \tag{18}$$

We also note that the QC mapping no. 1 and mapping no. 2 approximations for $\hat{Q}_a$, eq 8, are given by

$$[\hat{Q}_a]_W^{(I)}(\mathbf{q}, \mathbf{p}) = N_e[\hat{M}_{aa}]_W^{(I)}(\mathbf{q}, \mathbf{p}) - \sum_{b=1}^{N_e}[\hat{M}_{bb}]_W^{(I)}(\mathbf{q}, \mathbf{p})$$
$$[\hat{Q}_a]_W^{(II)}(\mathbf{q}, \mathbf{p}) = N_e[\hat{M}_{aa}]_W^{(II)}(\mathbf{q}, \mathbf{p}) - \sum_{b=1}^{N_e}[\hat{M}_{bb}]_W^{(II)}(\mathbf{q}, \mathbf{p}) \tag{19}$$

Applying the above-mentioned QC/MH approximations to eqs 11 or 12 yields the five different LSC-based methods shown in Table 1 (see refs 56 and 48 for a more detailed discussion). The first two methods, LSCI (also referred to as PBME[63]) and LSCII (also referred to as LSC-IVR[39]) are based on eq 11. Both LSCI and LSCII use mapping no. 2 for $[\hat{M}_{\alpha\alpha}]_W$ but differ from each other in the mapping used for $[\hat{M}_{kj}]_W$, with LSCI using mapping no. 1 and LSCII using mapping no. 2.

Table 1. Summary of the Five LSC-Based QC/MH Methods Used in This Paper[a]

Methods Using $\sigma(t)$ Based on Eq 11		
	$C_{[\hat{M}_{\alpha\alpha}]_W[\hat{M}_{kj}]_W}(t)$	
method	$[\hat{M}_{\alpha\alpha}]_W$ mapping	$[\hat{M}_{kj}]_W$ mapping
LSCI	$[\hat{M}_{\alpha\alpha}]_W^{(II)}(\mathbf{q},\mathbf{p})$	$[\hat{M}_{kj}]_W^{(I)}(\mathbf{q},\mathbf{p})$
LSCII	$[\hat{M}_{\alpha\alpha}]_W^{(II)}(\mathbf{q},\mathbf{p})$	$[\hat{M}_{kj}]_W^{(II)}(\mathbf{q},\mathbf{p})$

Methods Using $\sigma(t)$ Based on Eq 12				
	$C_{[\hat{A}]_W[\hat{B}]_W}(t)$			
	$[\hat{A}]_W$		$[\hat{B}]_W$	
method	$[\hat{1}]_W$ mapping	$[\hat{Q}_\lambda]_W$ mapping	$[\hat{Q}_\alpha]_W$ mapping	$[\hat{M}_{kj}]_W$ mapping
mLSC/$\phi^1\phi^1$	1	$[\hat{Q}_\lambda]_W^{(I)}(\mathbf{q},\mathbf{p})$	$[\hat{Q}_\lambda]_W^{(II)}(\mathbf{q},\mathbf{p})$	$[\hat{M}_{kj}]_W^{(II)}(\mathbf{q},\mathbf{p})$
mLSC/$\phi^1\phi^2$	1	$[\hat{Q}_\lambda]_W^{(II)}(\mathbf{q},\mathbf{p})$	$[\hat{Q}_\lambda]_W^{(II)}(\mathbf{q},\mathbf{p})$	$[\hat{M}_{kj}]_W^{(II)}(\mathbf{q},\mathbf{p})$
mLSC/$\phi^2\phi^2$	$2\hbar\phi(\mathbf{q}, \mathbf{p})$	$[\hat{Q}_\lambda]_W^{(II)}(\mathbf{q},\mathbf{p})$	$[\hat{Q}_\lambda]_W^{(II)}(\mathbf{q},\mathbf{p})$	$[\hat{M}_{kj}]_W^{(II)}(\mathbf{q},\mathbf{p})$

[a] $[\hat{M}]_W^I$ is given in eq 16, $[\hat{M}]_W^{II}$ is given in eq 17, $[\hat{Q}]_W$ is given in eq 19, $\phi(\mathbf{q}, \mathbf{p})$ is given in eq 18, and the general form of $C_{A_WB_W}(t)$ is given in eq 14.

The third through fifth LSC-based methods are based on eq 12 and were recently introduced by Saller et al.[48] For the correlation functions $C_{[\hat{1}]_W[\hat{Q}_\lambda]_W}$, $C_{[\hat{1}]_W[\hat{M}_{\zeta\lambda}]_W}$, $C_{[\hat{Q}_\alpha]_W[\hat{Q}_\lambda]_W}$, and $C_{[\hat{Q}_\alpha]_W[\hat{M}_{\zeta\lambda}]_W}$ [see eq 12], all three methods use mapping no. 2 for $[\hat{Q}_\lambda]_W$ and $[\hat{M}_{\zeta\lambda}]_W$ but differ in how they map the unity operator and in the mapping used for $[\hat{Q}_\alpha]_W$. The third method, referred to as mLSC/$\phi^1\phi^1$, maps the unity operator onto 1 and uses mapping no. 1 for $[\hat{Q}_\alpha]_W$. The fourth method, referred to as mLSC/$\phi^1\phi^2$, maps the unity operator onto 1 and uses mapping no. 2 for $[\hat{Q}_\alpha]_W$. The fifth method, referred to as

https://dx.doi.org/10.1021/acs.jctc.0c00177
J. Chem. Theory Comput. XXXX, XXX, XXX−XXX

mLSC/$\phi^2\phi^2$, maps the unity operator onto $2\hbar\phi(\mathbf{q}, \mathbf{p})$ [with $\phi(\mathbf{q}, \mathbf{p})$ given in eq 18] and uses mapping no. 2 for $[\hat{Q}_\alpha]_W$.

In order to obtain the correlation functions in eqs 11 and 12, the nuclear and electronic coordinates and momenta at time t, $\{\mathbf{R}_t, \mathbf{P}_t, \mathbf{q}_t, \mathbf{p}_t\}$, need to be obtained from the initial state $\{\mathbf{R}_0, \mathbf{P}_0, \mathbf{q}_0, \mathbf{p}_0\}$. The initial nuclear coordinates and momenta are sampled from the Wigner transform of the initial nuclear density matrix, $\hat{\rho}_n(0) = e^{-\beta\hat{H}_\alpha}/\mathrm{Tr}\{e^{-\beta\hat{H}_\alpha}\}$:

$$[\hat{\rho}_n(0)]_W(\mathbf{R}_0, \mathbf{P}_0) = \prod_{i=1}^{N_n} \frac{\tanh(\beta\hbar\omega_i/2)}{\pi\hbar} \times \exp\left[-\frac{2\tanh(\beta\hbar\omega_i/2)}{\hbar\omega_i}\left(\Delta_\alpha + \frac{P_i^2}{2} + \frac{1}{2}\omega_i^2 R_i^2 + d_i^{(\alpha)} R_i\right)\right] \tag{20}$$

The initial electronic coordinates and momenta are sampled based on the phase-space density $\phi(\mathbf{q}_0, \mathbf{p}_0)$ (see Table 1).

$\{\mathbf{R}_t, \mathbf{P}_t, \mathbf{q}_t, \mathbf{p}_t\}$ is obtained from $\{\mathbf{R}_0, \mathbf{P}_0, \mathbf{q}_0, \mathbf{p}_0\}$ via classical dynamics as dictated by the following symmetrized mapping Hamiltonian[13,41]

$$H(\mathbf{R}, \mathbf{P}, \mathbf{q}, \mathbf{p}) = \frac{\mathbf{P}^2}{2} + \bar{V}(\mathbf{R}) + \frac{1}{2\hbar}\sum_{j=1}^{N_e}[V_{jj}(\mathbf{R}) - \bar{V}(\mathbf{R})] \times (q_j^2 + p_j^2) + \frac{1}{2\hbar}\sum_{\substack{j,k=1 \\ k\neq j}}^{N_e} V_{jk}(\mathbf{R})(q_j - ip_j)(q_k + ip_k) \tag{21}$$

It should be noted that the symmetrized form of the mapping Hamiltonian, eq 21, is obtained by rewriting $V_{jj}(\mathbf{R})$ as $\bar{V}(\mathbf{R}) + [V_{jj}(\mathbf{R}) - \bar{V}(\mathbf{R})]$, where $\bar{V}(\mathbf{R}) = \frac{1}{N_e}\sum_{j=1}^{N_e} V_{jj}(\mathbf{R})$, and using the closure relation, $\sum_{j=1}^{N_e}|j\rangle\langle j| = \hat{1}$. Details on the numerical integration scheme are described in Appendix A.

3.2. The Symmetrical Quasiclassical (SQC) Method.

The symmetrical quasiclassical (SQC) method can also be viewed as an alternative implementation of the LSC approximation.[42−47] This method is formulated in terms of action-angle (a-a) variables rather than in terms of Cartesian coordinates and momenta. Each electronic state $|j\rangle$ is associated with a *classical* harmonic mode whose state is described by an action variable, n_j, and an angle variable, u_j.[13,64] The QC mapping variables for the electronic density matrix elements in terms of a-a variables are given by

$$[\hat{M}_{\lambda\lambda}]_W^{(\mathrm{SQC})}(\mathbf{n}, \mathbf{u}) = \delta(n_\lambda - 1)\prod_{\substack{\xi=1 \\ \xi\neq\lambda}}^{N_e}\delta(n_\xi),$$

$$[\hat{M}_{\lambda\zeta}]_W^{(\mathrm{SQC})}(\mathbf{n}, \mathbf{u}) = e^{i(u_\zeta - u_\lambda)}\delta\left(n_\lambda - \frac{1}{2}\right) \times \delta\left(n_\zeta - \frac{1}{2}\right)\prod_{\substack{\xi=1 \\ \xi\neq\lambda,\zeta}}^{N_e}\delta(n_\xi) \tag{22}$$

where $\mathbf{n} = (n_1, ..., n_{N_e})$ and $\mathbf{u} = (u_1, ..., u_{N_e})$. The SQC method is based on replacing the delta functions in eq 22 with prelimit delta functions. In this work, we use two different choices that lead to square sampling windows and triangular sampling windows.[46]

For the square sampling windows, $\delta(n_j - a)$ is replaced with $h(\gamma - |n_j - a|)/2\gamma$, where

$$h(x) = \begin{cases} 1 & x \geq 0 \\ 0 & x < 0 \end{cases} \tag{23}$$

is the Heaviside function. This gives mapping variables for two-state systems of the form

$$[\hat{M}_{\lambda\lambda}]_W^{(\mathrm{SQC\text{-}square})}(\mathbf{n}, \mathbf{u}) = h(\gamma - |n_\lambda - 1|)h(\gamma - |n_\zeta|)$$

$$[\hat{M}_{\lambda\zeta}]_W^{(\mathrm{SQC\text{-}square})}(\mathbf{n}, \mathbf{u}) = e^{i(u_\zeta - u_\lambda)}h\left(\gamma - \left|n_\lambda - \frac{1}{2}\right|\right) \times h\left(\gamma - \left|n_\zeta - \frac{1}{2}\right|\right) \tag{24}$$

where γ is the window width parameter. The value of the window width parameter, γ, is set to 0.366, as recommended in ref 42.

For triangular sampling windows, the mapping variables for two-state systems are given by

$$[\hat{M}_{\lambda\lambda}]_W^{(\mathrm{SQC\text{-}triangle})}(\mathbf{n}, \mathbf{u}) = 2h(n_\lambda + \gamma - 1)h(n_\zeta + \gamma) \times h(2 - 2\gamma - n_\lambda - n_\zeta)$$

$$[\hat{M}_{\lambda\zeta}]_W^{(\mathrm{SQC\text{-}triangle})}(\mathbf{n}, \mathbf{u}) = 2e^{i(u_\zeta - u_\lambda)}h\left(n_\lambda + \gamma - \frac{1}{2}\right) \times h\left(n_\zeta + \gamma - \frac{1}{2}\right)h(2 - 2\gamma - n_\lambda - n_\zeta) \tag{25}$$

Previous studies[46] showed that using triangular sampling windows gives rise to more accurate results and better convergence compared to using square sampling windows.

Within SQC, initial nuclear coordinates and momenta are sampled based on $[\hat{\rho}_n(0)]_W(\mathbf{R}_0,\mathbf{P}_0)$, given in eq 20 (the same as in LSC-based methods). In the case of a system with an initial electronic state $\hat{\sigma}(0)=|\alpha\rangle\langle\alpha|$, for square windows, initial sampling of the action variable, n_l, is done randomly within the intervals

$$\begin{cases} (1-\gamma, 1+\gamma) & l = \alpha \\ (-\gamma, \gamma) & l \neq \alpha \end{cases} \tag{26}$$

For triangle windows, n_l is sampled randomly within the intervals

$$\begin{cases} (1-\gamma, 2-\gamma) & l = \alpha \\ (-\gamma, 1-\gamma) & l \neq \alpha \end{cases} \tag{27}$$

subject to the constraint $n_\lambda + n_\zeta \leq 2 - 2\gamma$. For both square and triangle mapping variables, initial sampling of the angle variables, $\{u_1, u_2\}$, is done randomly within the interval $(0, 2\pi)$.

The dynamics of the a-a variables within SQC is done in terms of Cartesian coordinates and momenta and is identical to that in the LSC-based methods. The relationship between the a-a variables and the Cartesian coordinates and momenta is given by

$$q_l = \sqrt{2(n_l + \gamma)\hbar}\,\cos(u_l)$$

$$p_l = \sqrt{2(n_l + \gamma)\hbar}\,\sin(u_l) \tag{28}$$

It should be noted that another implementation of the SQC method, which allows for a trajectory-dependent definition of γ, was recently shown to be significantly more accurate when applied to a one-dimensional photodissociation model.[70] However, application of this new version of SQC was observed

https://dx.doi.org/10.1021/acs.jctc.0c00177
J. Chem. Theory Comput. XXXX, XXX, XXX−XXX

not to produce significant improvement over the SQC with a fixed γ and triangular sampling windows for the systems under consideration in this work (not shown).

3.3. The Mean-Field (Ehrenfest) Method. The mean-field (MF) method can also be cast as a QC/MH-type method[13] by expanding the electronic wave function at time t in the electronic basis, $\{|j\rangle\}$,

$$|\psi(t)\rangle = \sum_{j=1}^{N_e} c_j(t)|j\rangle \tag{29}$$

and expressing the expansion coefficients in terms of Cartesian coordinates and momenta as follows

$$c_j = \frac{1}{\sqrt{2}}(q_j + ip_j) \tag{30}$$

The corresponding electronic density matrix is given by

$$\hat{\sigma}(t) = |\psi(t)\rangle\langle\psi(t)| = \sum_{j,k=1}^{N_e} c_j(t)c_k^*(t)|j\rangle\langle k| \tag{31}$$

It can then be shown that the MF method is equivalent to propagating $\{\mathbf{R}_t, \mathbf{P}_t, \mathbf{q}_t, \mathbf{p}_t\}$ as classical variables whose dynamics is governed by the QC Hamiltonian in eq 21.[13] The initial nuclear coordinates and momenta within the MH method are sampled in the same way as the LSC and SQC methods [see eq 20]. However, unlike the LSC and SQC methods, the initial values of the electronic coordinates and momenta, $\{\mathbf{q}_0, \mathbf{p}_0\}$ are uniquely determined by $c_j(0)$.

4. RESULTS

In this section, we report the results of calculations performed on the LVC model for three sets of parameters that correspond to the following three gas-phase molecules: fulvene, the 2,6-bis(methylene) adamantyl (BMA) radical cation, and the 2-methylene-6-isopropylidene adamantyl (MIA) radical cation. Those parameters were adopted from ref 5, where they were obtained from electronic structure calculations and the Köppel diabatization scheme.[71−73] Several key model parameters for the three molecules are shown in Table 2. It should be noted that fulvene corresponds to the Marcus inverted region ($|\Delta E| > E_r$), while BMA and MIA correspond to the Marcus normal region ($|\Delta E| < E_r$).

Table 2. Number of Nuclear Modes, Absolute Value of the Reaction Free Energy, $|\Delta E|$, and Reorganization Energy, E_r, for Fulvene, BMA, and MIA[a]

	fulvene	BMA	MIA
no. modes	30	78	96
$\|\Delta E\|$ (au)	0.0989	0.0004	0.0250
E_r (au)	0.0887	0.0297	0.0274

[a]Values adopted from ref 5.

We compare results obtained by applying the above-mentioned seven QC/MH methods (LSCI, LSCII, mLSC/$\phi^1\phi^1$, mLSC/$\phi^1\phi^2$, mLSC/$\phi^2\phi^2$, SQC, and MF) with quantum-mechanically exact results obtained via multilayer multiconfiguration time-dependent Hartree (ML-MCTDH).[15,74] Previously reported results for the same models via NE-FGR[58] are also included for comparison. The results shown for all methods, except for LSCI, were obtained by averaging over 10^6 trajectories. LSCI results were obtained by averaging over 5×10^7 trajectories. It should be noted that the number of trajectories needed for achieving convergence in the systems under consideration is somewhat larger than that needed for achieving convergence in previously considered models.[48,56,69] In the case of BMA and MIA, we believe that this is caused by the smaller overall change in the population over the time scale under consideration, which requires a smaller absolute error in order to reach the same tolerance with respect to the relative error. In the case of fulvene, we believe that this is caused by the highly nonequilibrium nature of the initial state. This results in stepwise population relaxation, which implies that much of the population relaxation happens before the system is able to reach equilibrium on the donor PES.

We also note that the MCTDH results reported below are somewhat different from previously reported results obtained via the variational multiconfigurational Gaussian (vMCG) wave packet method[5] (not shown). While the origin of this discrepancy is difficult to ascertain, we speculate that they may reflect an insufficiently large Gaussian basis set used to obtain the vMCG results.

4.1. Fulvene Molecule. The results for fulvene are shown in Figure 1. In this case, $\hat{\sigma}(0) = |2\rangle\langle 2|$ and $\hat{\rho}_n(0) = e^{-\beta\hat{H}_1}/\mathrm{Tr}\{e^{-\beta\hat{H}_1}\}$ (the electronic states are as labeled in ref 5).

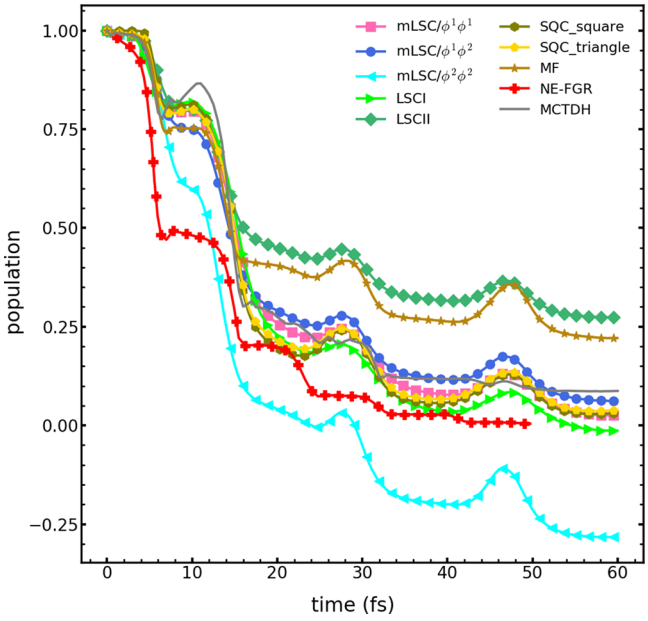

Figure 1. Comparison of donor population dynamics for the gas-phase fulvene molecule via different methods at $T = 0$. The MCTDH results, represented by a black line, give the exact dynamics for fulvene with the LVC model.

We first note that while NE-FGR follows a similar trend to that of MCTDH, there are significant quantitative deviations between the two, with NE-FGR overestimating the electronic transition rate. This suggests a breakdown of the weak electronic coupling approximation underlying NE-FGR and the necessity of a post-FGR method for quantitatively predicting electronic transition rates for this molecule.

MF, which is arguably the simplest such post-FGR method, is seen to reproduce the MCTDH electronic transition rate rather well at short times but to significantly underestimate the electronic transition rate at longer times. LSCII is seen to

https://dx.doi.org/10.1021/acs.jctc.0c00177
J. Chem. Theory Comput. XXXX, XXX, XXX−XXX

follow a similar behavior to MF and is in fact slightly worse than MF at longer times. LSCI, on the other hand, is seen to reproduce the MCTDH result rather well throughout the entire time range.

Among the modified LSC methods, mLSC/$\phi^1\phi^1$ and mLSC/$\phi^1\phi^2$ are seen to reproduce the MCTDH result rather well throughout the entire time range, with mLSC/$\phi^1\phi^1$ performing slightly better than mLSC/$\phi^1\phi^2$. At the same time, mLSC/$\phi^2\phi^2$ is seen to not only significantly overestimate the electronic transition rate beyond very short times, but also predict a negative electronic population at longer times, which is clearly nonphysical.

Finally, SQC, with either square or triangular sampling windows, is seen to reproduce the MCTDH result rather well throughout the entire time range and is in fact very close to the best performing modified LSC method, mLSC/$\phi^1\phi^1$.

4.2. 2,6-Bis(methylene) Adamantyl (BMA) Radical Cation. The results for BMA are shown in Figure 2. In this case, $\hat{\sigma}(0) = |1\rangle\langle 1|$ and $\hat{\rho}_n(0) = e^{-\beta\hat{H}_2}/\mathrm{Tr}\{e^{-\beta\hat{H}_2}\}$ (the electronic states are as labeled in ref 5).

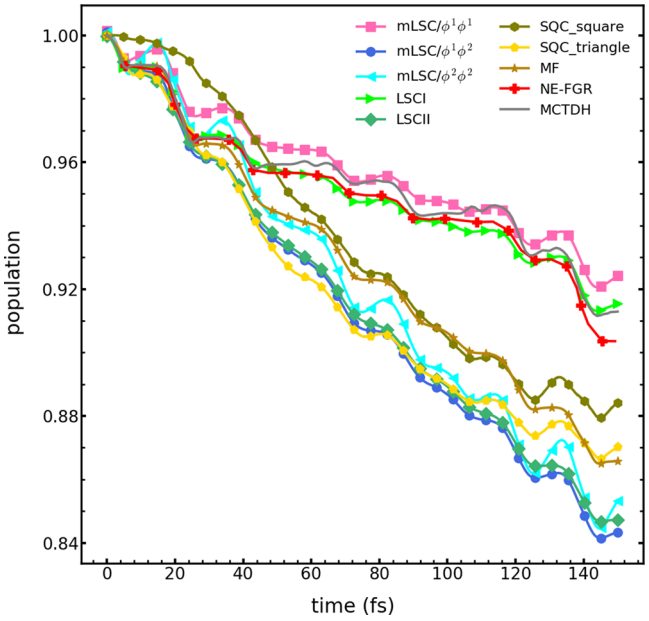

Figure 2. Comparison of donor population dynamics for the gas-phase BMA radical cation via different methods at $T = 0$. The MCTDH results, represented by a black line, give the exact dynamics for BMA with the LVC model.

For BMA, NE-FGR reproduces the MCTDH result rather well, implying that the weak electronic coupling approximation underlying NE-FGR is valid and, given its relative simplicity, may in fact be the method of choice for this molecule.

At the same time, MF is seen to deviate significantly from the MCTDH result and to actually overestimate the electronic transition rate. LSCII is seen to follow a similar behavior to MF and is in fact somewhat worse than MF at longer times. In contrast, and similarly to fulvene, LSCI is seen to reproduce the MCTDH result rather well throughout the entire time range.

Among the modified LSC methods, only mLSC/$\phi^1\phi^1$ is seen to reproduce the MCTDH result rather well throughout the entire time range, while mLSC/$\phi^1\phi^2$ and mLSC/$\phi^2\phi^2$ are seen to significantly overestimate the MCTDH electronic transition rate. In fact, the quality of the mLSC/$\phi^1\phi^1$ result is seen to be comparable to that of LSCI, while that of the mLSC/$\phi^1\phi^2$ and mLSC/$\phi^2\phi^2$ is comparable to that of LSCII.

Finally, the SQC result for BMA is seen to be of comparable quality to that of MF and is therefore relatively inaccurate. Furthermore, significant deviations are observed between SQC results obtained with square or triangular sampling windows.

4.3. 2-Methylene-6-isopropylidene Adamantyl (MIA) Radical Cation. The results for MIA are shown in Figure 3. In this case, $\hat{\sigma}(0) = |1\rangle\langle 1|$ and $\hat{\rho}_n(0) = e^{-\beta\hat{H}_2}/\mathrm{Tr}\{e^{-\beta\hat{H}_2}\}$ (the electronic states are as labeled in ref 5).

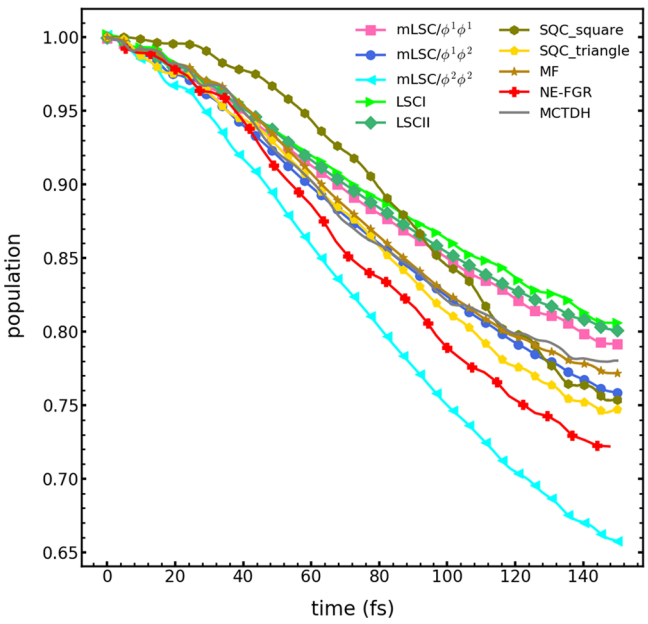

Figure 3. Comparison of donor population dynamics for the gas-phase MIA radical cation via different methods at $T = 0$. The MCTDH results, represented by a black line, give the exact dynamics for MIA with the LVC model.

NE-FGR is seen to somewhat overestimate the electronic transition rate in MIA, which suggests a breakdown of the weak electronic coupling approximation, although to a lesser extent than in the case of fulvene.

Interestingly, the MF result is in excellent agreement with the MCTDH result for this molecule, which stands in sharp contrast to the poor performance of MF in fulvene and BMA. Also in contrast to fulvene and BMA, LSCI and LSCII yield rather similar results in this case, which are in reasonable agreement with MCTDH, but clearly not as accurate as MF.

Among the modified LSC methods, mLSC/$\phi^1\phi^1$, and mLSC/$\phi^1\phi^2$ are seen to reproduce the MCTDH result rather well throughout the entire time range under consideration, with mLSC/$\phi^1\phi^2$ yielding similar accuracy to MF and being somewhat more accurate than mLSC/$\phi^1\phi^1$. At the same time, and similarly to fulvene and BMA, mLSC/$\phi^2\phi^2$ is seen to significantly overestimate the electronic transition rate, with the deviation increasing with increasing time.

Finally, while the SQC results are seen to agree reasonably well with the MCTDH result, using triangular sampling windows clearly yields a more accurate transition rate compared to using square windows. Furthermore, the quality of the results obtained via SQC with triangular sampling

https://dx.doi.org/10.1021/acs.jctc.0c00177
J. Chem. Theory Comput. XXXX, XXX, XXX−XXX

windows is seen to be comparable to that of MF and mLSC/$\phi^1\phi^2$.

5. DISCUSSION

For the sake of comparing the performance of the different methods over the three systems they were applied to, we classify them as *accurate* ($\surd$) and *inaccurate* ($\times$) based on their ability to reproduce the MCTDH results over the time range under consideration. A summary of the performance of the different methods based on this classification is give in Table 3.

Table 3. Summary of Results[a]

	method				
	LSCI	LSCII	mLSC/$\phi^1\phi^1$	mLSC/$\phi^1\phi^2$	mLSC/$\phi^2\phi^2$
fulvene	$\surd$	$\times$	$\surd$	$\surd$	$\times$
BMA	$\surd$	$\times$	$\surd$	$\times$	$\times$
MIA	$\surd$	$\surd$	$\surd$	$\surd$	$\times$
	method				
	SQC square		SQC triangle	MF	NE-FGR
fulvene	$\surd$		$\surd$	$\times$	$\times$
BMA	$\times$		$\times$	$\times$	$\surd$
MIA	$\times$		$\surd$	$\surd$	$\times$

[a] $\surd$ implies that the method is accurate, and $\times$ implies that the method is inaccurate.

It should be noted that classifying the methods as accurate and inaccurate is somewhat subjective and obviously cannot account for more nuanced behavior (e.g., methods that are accurate at short time but whose accuracy deteriorates at longer times). However, given the large number of methods, we believe that it serves as a useful organizational tool to guide the following discussion.

Based on the aforementioned classification of methods as *accurate* and *inaccurate*, they can be grouped into three categories: (1) methods that are consistently accurate for all three molecules, (2) methods that are consistently inaccurate for all molecules, and (3) methods with inconsistent accuracy, which are accurate for some molecules but inaccurate for others.

mLSC/$\phi^1\phi^1$ and LSCI fall into the first category (accurate for all three molecules). The fact that mLSC/$\phi^1\phi^1$ is seen to be somewhat more accurate and LSCI has been previously observed to be significantly less accurate than mLSC/$\phi^1\phi^1$ for other benchmark models[49,56] points to mLSC/$\phi^1\phi^1$ as the method of choice.

mLSC/$\phi^2\phi^2$ is the only method that falls into the second category (inaccurate for all three molecules). The poor performance of mLSC/$\phi^2\phi^2$ is particularly surprising in light of its previously reported ability to produce accurate results for the spin-boson and Tully models.[56] This observation underscores the limitations of those popular benchmark models and the need for extending the testing of approximate methods to other benchmark models, such as the LVC model considered here. It should also be noted that unlike mLSC/$\phi^1\phi^1$ and mLSC/$\phi^1\phi^2$, the derivation of mLSC/$\phi^2\phi^2$ is somewhat ad-hoc.

The remaining methods fall into the third category. Within this category, one can distinguish between two subcategories: (3A) methods that are accurate for two out of the three molecules and (3B) methods that are accurate for one out of the three molecules.

Two methods fall into category 3A, namely, mLSC/$\phi^1\phi^2$ and SQC with triangular windows. Both methods are seen to only be inaccurate in the case of BMA, which is also the only molecule for which NE-FGR is seen to be accurate. This correlation between weak electronic coupling and inaccuracy of mapping methods has been previously pointed out in the context of SQC.[47] The problem has been traced back to inefficient transfer of classical trajectories from one sampling window to another when the electronic coupling is weak. Switching from SQC with square sampling windows to SQC with triangular sampling windows was proposed in ref 47 as a remedy for this problem. Interestingly, the poor performance of SQC with either square or triangular windows seems to suggest that this remedy is not sufficient in the case of BMA. The fact that unlike SQC, mLSC/$\phi^1\phi^1$ and LSCI are seen to be accurate for BMA can be traced back to the lack of a window function at time t in both, which guarantees that contributions from all trajectories are accounted for (as opposed to only accounting for contributions from trajectories that manage to transfer from one sampling window to another).

Finally, category 3B includes the MF and SQC with square sampling windows methods. The only system for which MF is accurate is MIA, which can be attributed to the fact that MIA is the system with the smallest barrier and largest number of nuclear modes. As a result, the MF approximation is expected to be more valid. The failure of SQC with square sampling windows to reproduce the MCTDH result in BMA can be traced back to the weak electronic coupling in this system (see discussion above). The behavior of SQC with square sampling windows in the case of MIA is more subtle. On the one hand, the actual transition rate constant, as measured by the slope of the population as a function of time, is comparable to the exact one. On the other hand, there appears to be a delay in establishing rate kinetics within SQC with square sampling windows, which can be traced back to the gap between sampling windows in action space. More specifically, there is lag time between the time a trajectory leaves one sampling window and the time it reaches another.

6. CONCLUDING REMARKS

Our main goal in this article was to extend the testing of QC/MH methods to systems with CIs. One reason for doing so is the central role CIs play in many photochemical processes of practical interest. Another reason is the need to extend the testing of those methods beyond the popular spin-boson and Tully benchmark models. Indeed, using the LVC model as a benchmark demonstrates the importance of going beyond the spin-boson and Tully models. More specifically, application of QC/MH methods to the LVC model was found to shed new light on the ability of those methods to yield accurate results. On the one hand, methods like SQC and mLSC/$\phi^2\phi^2$ were found to be significantly less accurate in LVC than they were in the spin-boson and Tully models. On the other hand, a method like mLSC/$\phi^1\phi^1$ was seen to emerge as the method of choice due its reasonable accuracy for all benchmark models.

It should be noted that the analysis presented in this article was performed on systems with relatively high vibrational frequencies at zero temperature, which corresponds to the most challenging test for a QC method due to the pronounced quantum nature of the system under those conditions. On the one hand, it is encouraging to see that at least some QC/MH methods are accurate under those extreme conditions. On the

https://dx.doi.org/10.1021/acs.jctc.0c00177
J. Chem. Theory Comput. XXXX, XXX, XXX−XXX

other hand, one expects the accuracy of the other methods to improve with increasing temperatures. Another way of enhancing the accuracy of QC/MH methods is by limiting their use to calculating the memory kernel of the generalized quantum master equation (GQME).[69,75] Work on those extensions is underway in our group and will be reported in future publications.

A. NUMERICAL INTEGRATION FOR QC/MH METHODS

In this appendix, we outline the numerical integration scheme we used for QC/MH methods.

For each propagation time step, we first propagate the nuclear DOF with the velocity Verlet algorithm. Then we apply the fourth-order Runge−Kutta method with self-adjusted step size to propagate the electronic DOF. This is done by setting a threshold error value ϵ and iteratively decreasing step size by half until the following inequality holds for all $i = 1, 2, ..., N_e$:

$$\Delta q_i = \left| q_i(t+dt) - q_i\left(\left[t+\frac{dt}{2}\right]+\frac{dt}{2}\right)\right| \le \epsilon$$
$$\Delta p_i = \left| p_i(t+dt) - p_i\left(\left[t+\frac{dt}{2}\right]+\frac{dt}{2}\right)\right| \le \epsilon \quad (32)$$

Here, $q(t+dt)$ represents propagating q by one step with step size equal to dt and $q_i\left(\left[t+\frac{dt}{2}\right]+\frac{dt}{2}\right)$ represents propagating q by two steps with each step size equal to $\frac{dt}{2}$. We used a threshold error value of $\epsilon = 0.01$. Considering the fact that nuclear DOF move much slower than electronic DOF, we obtain the intermediate nuclear DOF information that is required for propagation of electronic DOF via linear interpolation.

AUTHOR INFORMATION

Corresponding Author

Eitan Geva − *Department of Chemistry, University of Michigan, Ann Arbor, Michigan 48109, United States;* orcid.org/0000-0002-7935-4586; Email: eitan@umich.edu

Authors

Yudan Liu − *Department of Chemistry, University of Michigan, Ann Arbor, Michigan 48109, United States*

Xing Gao − *Department of Chemistry, University of Michigan, Ann Arbor, Michigan 48109, United States*

Yifan Lai − *Department of Chemistry, University of Michigan, Ann Arbor, Michigan 48109, United States*

Ellen Mulvihill − *Department of Chemistry, University of Michigan, Ann Arbor, Michigan 48109, United States*

Complete contact information is available at: https://pubs.acs.org/10.1021/acs.jctc.0c00177

Notes

The authors declare no competing financial interest.

ACKNOWLEDGMENTS

We are grateful for support from NSF via Grant CHE-1800325 and computational resources and services provided by Advanced Research Computing at the University of Michigan, Ann Arbor.

REFERENCES

(1) Domcke, W.; Yarkony, D. R.; Köppel, H. *Conical Intersections*; World Scientific, 2004.

(2) Worth, G. A.; Cederbaum, L. S. Beyond Born-Oppenheimer: Molecular Dynamics Through a Conical Intersection. *Annu. Rev. Phys. Chem.* **2004**, *55*, 127−158.

(3) Köppel, H.; Domcke, W.; Cederbaum, L. S. *Conical Intersections*; World Scientific, 2004; pp 323−367.

(4) Levine, B. G.; Martínez, T. J. Isomerization Through Conical Intersections. *Annu. Rev. Phys. Chem.* **2007**, *58*, 613−634.

(5) Izmaylov, A. F.; Mendive-Tapia, D.; Bearpark, M. J.; Robb, M. A.; Tully, J. C.; Frisch, M. J. Nonequilibrium Fermi golden rule for electronic transitions through conical intersections. *J. Chem. Phys.* **2011**, *135*, 234106.

(6) Deb, S.; Weber, P. M. The Ultrafast Pathway of Photon-Induced Electrocyclic Ring-Opening Reactions: The Case of 1,3-Cyclohexadiene. *Annu. Rev. Phys. Chem.* **2011**, *62*, 19−39.

(7) Matsika, S.; Krause, P. Nonadiabatic Events and Conical Intersections. *Annu. Rev. Phys. Chem.* **2011**, *62*, 621−643.

(8) Domcke, W.; Yarkony, D.R.; Köppel, H. *Conical Intersections: Theory, Computation and Experiment*; World Scientific: Singapore, 2011.

(9) Domcke, W.; Yarkony, D. R. Role of Conical Intersections in Molecular Spectroscopy and Photoinduced Chemical Dynamics. *Annu. Rev. Phys. Chem.* **2012**, *63*, 325−352.

(10) Endicott, J. S.; Joubert-Doriol, L.; Izmaylov, A. F. A perturbative formalism for electronic transitions through conical intersections in a fully quadratic vibronic model. *J. Chem. Phys.* **2014**, *141*, 034104.

(11) Shu, Y.; Levine, B. G. Nonradiative Recombination via Conical Intersections Arising at Defects on the Oxidized Silicon Surface. *J. Phys. Chem. C* **2015**, *119*, 1737−1747.

(12) Gherib, R.; Ryabinkin, I. G.; Izmaylov, A. F. Why Do Mixed Quantum-Classical Methods Describe Short-Time Dynamics through Conical Intersections So Well? Analysis of Geometric Phase Effects. *J. Chem. Theory Comput.* **2015**, *11*, 1375−1382.

(13) Meyer, H. D.; Miller, W. H. A classical analog for electronic degrees of freedom in nonadiabatic collision processes. *J. Chem. Phys.* **1979**, *70*, 3214−3223.

(14) Kosloff, R. Propagation methods for quantum molecular dynamics. *Annu. Rev. Phys. Chem.* **1994**, *45*, 145.

(15) Meyer, H.-D.; Gatti, F.; Worth, G. A. *Multidimensional Quantum Dynamics; MCTDH Theory and Applications*; John Wiley & Sons, 2009.

(16) Greene, S. M.; Batista, V. S. Tensor-Train Split-Operator Fourier Transform (TT-SOFT) Method: Multidimensional Nonadiabatic Quantum Dynamics. *J. Chem. Theory Comput.* **2017**, *13*, 4034−4042.

(17) McLachlan, A. A variational solution of the time-dependent Schrodinger equation. *Mol. Phys.* **1964**, *8*, 39−44.

(18) Tully, J. C. Molecular dynamics with electronic transitions. *J. Chem. Phys.* **1990**, *93*, 1061−1071.

(19) Tully, J. C.; Preston, R. K. Trajectory surface hopping approach to nonadiabatic molecular collisions: Reaction of H^+ with D_2. *J. Chem. Phys.* **1971**, *55*, 562−572.

(20) Bittner, E. R.; Rossky, P. J. Quantum decoherence in mixed quantum-classical systems: Nonadiabatic processes. *J. Chem. Phys.* **1995**, *103*, 8130−8143.

(21) Prezhdo, O. V.; Rossky, P. J. Evaluation of quantum transition rates from quantum-classical molecular dynamics simulations. *J. Chem. Phys.* **1997**, *107*, 5863−5878.

(22) Horenko, I.; Salzmann, C.; Schmidt, B.; Schutte, C. Quantum-classical Liouville approach to molecular dynamics: Surface hopping Gaussian phase-space packets. *J. Chem. Phys.* **2002**, *117*, 11075−11088.

(23) Subotnik, J. E.; Shenvi, N. A new approach to decoherence and momentum rescaling in the surface hopping algorithm. *J. Chem. Phys.* **2011**, *134*, 024105−19.

https://dx.doi.org/10.1021/acs.jctc.0c00177
J. Chem. Theory Comput. XXXX, XXX, XXX−XXX

(24) Shushkov, P.; Li, R.; Tully, J. C. Ring polymer molecular dynamics with surface hopping. *J. Chem. Phys.* **2012**, *137*, 22A549.
(25) Wang, L.; Trivedi, D.; Prezhdo, O. V. Global Flux Surface Hopping Approach for Mixed Quantum-Classical Dynamics. *J. Chem. Theory Comput.* **2014**, *10*, 3598−3605.
(26) Jaeger, H. M.; Fischer, S.; Prezhdo, O. V. Decoherence-induced surface hopping. *J. Chem. Phys.* **2012**, *137*, 22A545.
(27) Wang, L.; Prezhdo, O. V. A Simple Solution to the Trivial Crossing Problem in Surface Hopping. *J. Phys. Chem. Lett.* **2014**, *5*, 713−719.
(28) Ouyang, W.; Dou, W.; Subotnik, J. E. Surface hopping with a manifold of electronic states. I. Incorporating surface-leaking to capture lifetimes. *J. Chem. Phys.* **2015**, *142*, 084109−13.
(29) Bedard-Hearn, M. J.; Larsen, R. E.; Schwartz, B. J. Mean-field dynamics with stochastic decoherence (MF-SD): A new algorithm for nonadiabatic mixed quantum/classical molecular-dynamics simulations with nuclear-induced decoherence. *J. Chem. Phys.* **2005**, *123*, 234106−17.
(30) Martens, C. C.; Fang, J. Semiclassical-limit molecular dynamics on multiple electronic surfaces. *J. Chem. Phys.* **1997**, *106*, 4918−4930.
(31) Donoso, A.; Martens, C. C. Simulation of coherent nonadiabatic dynamics using classical trajectories. *J. Phys. Chem. A* **1998**, *102*, 4291.
(32) Kapral, R.; Ciccotti, G. Mixed quantum-classical dynamics. *J. Chem. Phys.* **1999**, *110*, 8919−8929.
(33) Nielsen, S.; Kapral, R.; Ciccotti, G. Mixed quantum-classical surface hopping dynamics. *J. Chem. Phys.* **2000**, *112*, 6543−6553.
(34) Shi, Q.; Geva, E. A derivation of the mixed quantum-classical Liouville equation from the influence functional formalism. *J. Chem. Phys.* **2004**, *121*, 3393−3404.
(35) MacKernan, D.; Kapral, R.; Ciccotti, G. Sequential short-time propagation of quantum-classical dynamics. *J. Phys.: Condens. Matter* **2002**, *14*, 9069−9076.
(36) Mac Kernan, D.; Ciccotti, G.; Kapral, R. Trotter-Based Simulation of Quantum-Classical Dynamics. *J. Phys. Chem. B* **2008**, *112*, 424−432.
(37) Nassimi, A.; Bonella, S.; Kapral, R. Analysis of the quantum-classical Liouville equation in the mapping basis. *J. Chem. Phys.* **2010**, *133*, 134115−11.
(38) Stock, G.; Thoss, M. Semiclassical Description of Nonadiabatic Quantum Dynamics. *Phys. Rev. Lett.* **1997**, *78*, 578−581.
(39) Sun, X.; Wang, H.; Miller, W. H. Semiclassical theory of electronically nonadiabatic dynamics: Results of a linearized approximation to the initial value representation. *J. Chem. Phys.* **1998**, *109*, 7064.
(40) Swenson, D. W. H.; Levy, T.; Cohen, G.; Rabani, E.; Miller, W. H. Application of a semiclassical model for the second-quantized many-electron Hamiltonian to nonequilibrium quantum transport: The resonant level model. *J. Chem. Phys.* **2011**, *134*, 164103−9.
(41) Kelly, A.; van Zon, R.; Schofield, J.; Kapral, R. Mapping quantum-classical Liouville equation: Projectors and trajectories. *J. Chem. Phys.* **2012**, *136*, 084101−13.
(42) Cotton, S. J.; Miller, W. H. Symmetrical windowing for quantum states in quasi-classical trajectory simulations: Application to electronically non-adiabatic processes. *J. Chem. Phys.* **2013**, *139*, 234112−10.
(43) Cotton, S. J.; Miller, W. H. Symmetrical Windowing for Quantum States in Quasi-Classical Trajectory Simulations. *J. Phys. Chem. A* **2013**, *117*, 7190−7194.
(44) Cotton, S. J.; Igumenshchev, K.; Miller, W. H. Symmetrical windowing for quantum states in quasi-classical trajectory simulations: Application to electron transfer. *J. Chem. Phys.* **2014**, *141*, 084104−11.
(45) Cotton, S. J.; Miller, W. H. A Symmetrical Quasi-Classical Spin-Mapping Model for the Electronic Degrees of Freedom in Non-Adiabatic Processes. *J. Phys. Chem. A* **2015**, *119*, 12138−12145.
(46) Cotton, S. J.; Miller, W. H. The Symmetrical Quasi-Classical Model for Electronically Non-Adiabatic Processes Applied to Energy Transfer Dynamics in Site-Exciton Models of Light-Harvesting Complexes. *J. Chem. Theory Comput.* **2016**, *12*, 983−991.
(47) Cotton, S. J.; Miller, W. H. A new symmetrical quasi-classical model for electronically non-adiabatic processes: Application to the case of weak non-adiabatic coupling. *J. Chem. Phys.* **2016**, *145*, 144108.
(48) Saller, M. A. C.; Kelly, A.; Richardson, J. O. On the identity of the identity operator in nonadiabatic linearized semiclassical dynamics. *J. Chem. Phys.* **2019**, *150*, 071101.
(49) Saller, M. A. C.; Kelly, A.; Richardson, J. O. Improved population operators for multi-state nonadiabatic dynamics with the mixed quantum-classical mapping approach. *Faraday Discuss.* **2020**, *221*, 150−167.
(50) Tao, G. Electronically Nonadiabatic Dynamics in Singlet Fission: A Quasi-Classical Trajectory Simulation. *J. Phys. Chem. C* **2014**, *118*, 17299−17305.
(51) Tao, G. A multi-state trajectory method for non-adiabatic dynamics simulations. *J. Chem. Phys.* **2016**, *144*, 094108−9.
(52) Tao, G.; Shen, N. Mapping State Space to Quasiclassical Trajectory Dynamics in Coherence-Controlled Nonadiabatic Simulations for Condensed Phase Problems. *J. Phys. Chem. A* **2017**, *121*, 1734−1747.
(53) Tao, G. Nonadiabatic Dynamics of Hydrogen Diffusion on Cu(001): Classical Mapping Model with Multistate Projection Window in Real Space. *ChemPhysChem* **2019**, *20*, 2127.
(54) Liu, J. A unified theoretical framework for mapping models for the multi-state Hamiltonian. *J. Chem. Phys.* **2016**, *145*, 204105−15.
(55) He, X.; Liu, J. A new perspective for nonadiabatic dynamics with phase space mapping models. *J. Chem. Phys.* **2019**, *151*, 024105−22.
(56) Gao, X.; Saller, M. A. C.; Liu, Y.; Kelly, A.; Richardson, J. O.; Geva, E. Benchmarking Quasiclassical Mapping Hamiltonian Methods for Simulating Electronically Nonadiabatic Molecular Dynamics. *J. Chem. Theory Comput.* **2020**, *16*, 2883.
(57) Köppel, H.; Domcke, W.; Cederbaum, L. S. *Advances in Chemical Physics*; John Wiley & Sons, Ltd, 2007; pp 59−246.
(58) Sun, X.; Geva, E. Non-Condon nonequilibrium Fermi's golden rule rates from the linearized semiclassical method. *J. Chem. Phys.* **2016**, *145*, 064109−19.
(59) Thoss, M.; Stock, G. Mapping approach to the semiclassical description of nonadiabatic quantum dynamics. *Phys. Rev. A: At., Mol., Opt. Phys.* **1999**, *59*, 64−79.
(60) Stock, G.; Müller, U. Flow of zero-point energy and exploration of phase space in classical simulations of quantum relaxation dynamics. *J. Chem. Phys.* **1999**, *111*, 65−76.
(61) Miller, W. H. The semiclassical initial value representation: A potentially practical way for adding quantum effects to classical molecular dynamics simulations. *J. Phys. Chem. A* **2001**, *105*, 2942−2955.
(62) Ananth, N.; Venkataraman, C.; Miller, W. H. Semiclassical description of electronically nonadiabatic dynamics via the initial value representation. *J. Chem. Phys.* **2007**, *127*, 084114−10.
(63) Kim, H.; Nassimi, A.; Kapral, R. Quantum-classical Liouville dynamics in the mapping basis. *J. Chem. Phys.* **2008**, *129*, 084102.
(64) Miller, W. H.; Cotton, S. J. Communication: Wigner functions in action-angle variables, Bohr-Sommerfeld quantization, the Heisenberg correspondence principle, and a symmetrical quasi-classical approach to the full electronic density matrix. *J. Chem. Phys.* **2016**, *145*, 081102−5.
(65) Miller, W. H.; Cotton, S. J. Classical molecular dynamics simulation of electronically non-adiabatic processes. *Faraday Discuss.* **2016**, *195*, 9−30.
(66) Cotton, S. J.; Liang, R.; Miller, W. H. On the adiabatic representation of Meyer-Miller electronic-nuclear dynamics. *J. Chem. Phys.* **2017**, *147*, 064112−11.
(67) Wang, H.; Thoss, M.; Miller, W. H. Forward-backward initial value representation for the calculation of thermal rate constants for reactions in complex molecular systems. *J. Chem. Phys.* **2000**, *112*, 47.

https://dx.doi.org/10.1021/acs.jctc.0c00177
J. Chem. Theory Comput. XXXX, XXX, XXX−XXX

(68) Runeson, J. E.; Richardson, J. O. Spin-mapping approach for nonadiabatic molecular dynamics. *J. Chem. Phys.* **2019**, *151*, 044119.
(69) Mulvihill, E.; Gao, X.; Liu, Y.; Schubert, A.; Dunietz, B. D.; Geva, E. Combining the mapping Hamiltonian linearized semiclassical approach with the generalized quantum master equation to simulate electronically nonadiabatic molecular dynamics. *J. Chem. Phys.* **2019**, *151*, 074103.
(70) Cotton, S. J.; Miller, W. H. Trajectory-adjusted electronic zero point energy in classical Meyer-Miller vibronic dynamics: Symmetrical quasiclassical application to photodissociation. *J. Chem. Phys.* **2019**, *150*, 194110.
(71) Köppel, H.; Gronki, J.; Mahapatra, S. Construction scheme for regularized diabatic states. *J. Chem. Phys.* **2001**, *115*, 2377−2388.
(72) Köppel, H.; Schubert, B. The concept of regularized diabatic states for a general conical intersection. *Mol. Phys.* **2006**, *104*, 1069−1079.
(73) Allan, C. S. M.; Lasorne, B.; Worth, G. A.; Robb, M. A. A Straightforward Method of Analysis for Direct Quantum Dynamics: Application to the Photochemistry of a Model Cyanine. *J. Phys. Chem. A* **2010**, *114*, 8713−8729.
(74) Worth, G. A.; Beck, M. H.; Jäckle, A.; Vendrell, O.; Meyer, H.-D. *MCTDH Package*, version 8.2, (2000), version 8.3 (2002), version 8.4 (2007), version 8.5 (2013), version 8.5 contains the ML-MCTDH algorithm; Current versions 8.4.18 and 8.5.11 (2020). See http://mctdh.uni-hd.de/.
(75) Mulvihill, E.; Schubert, A.; Sun, X.; Dunietz, B. D.; Geva, E. A modified approach for simulating electronically nonadiabatic dynamics via the generalized quantum master equation. *J. Chem. Phys.* **2019**, *150*, 034101.

https://dx.doi.org/10.1021/acs.jctc.0c00177
J. Chem. Theory Comput. XXXX, XXX, XXX−XXX